

## Mechanical response of layered titanate nanowires

L. Rossi\*, R. Foschia, A. Glushkova, L. Forró, E. Horváth

Laboratory of Physics of Complex Matter, École Polytechnique Fédérale de Lausanne, 1015, Lausanne, Switzerland



### ARTICLE INFO

#### Keywords:

Layered ceramic  
Young modulus  
Shear modulus  
Fatigue

### ABSTRACT

The mechanical response of individual titanate nanowires ( $\text{H}_2\text{Ti}_3\text{O}_7$ ), synthesized in an upscaled production (kg/month) was investigated by means of an Atomic Force Microscope (AFM) in nanomechanical spectroscopic mode. Because of their layered structure, besides the Young's modulus ( $E$ ) of  $66.7 \pm 25$  GPa, an important contribution to the mechanical response was identified as coming from the low shear modulus ( $G$ ) of  $1.5 \pm 0.8$  GPa between the layers. The mechanical energy loss due to shear is at the origin of the material's fatigue, during which the individual titanate layers crack gradually, until the final failure of the structure. The high-temperature treatment at  $800^\circ\text{C}$  transforms the material into anatase ( $\text{TiO}_2$ ) nanowires, which have a considerably higher elastic modulus.

### 1. Introduction

$\text{TiO}_2$  nanoparticles, mostly in the anatase polymorph, are very popular in several applications, ranging from sunscreens to photovoltaic (PV) devices [1–4]. Their sister materials, the anatase nanowires (NWs) are equally interesting, gaining more and more emphasis in PV because of their higher dimensionality, the charge extraction is much more efficient. Beyond PV, they are used in photocatalytic water and air purification [5–10], in memristors [11], sensors [12,13], supercapacitors [14,15] and batteries [16]. Their precursor structures, from which they are obtained by thermal treatment, the titanates (e.g.  $\text{H}_2\text{Ti}_3\text{O}_7$ ), are equally important, as in the case when they are the active components of a very sensitive humidity sensor [17], they serve as reinforcement fibers in composites [18], super-insulation aerogels [19] or catalyst [20]. All these applications are getting credibility, since the synthesis from mg quantity by hydrothermal synthesis in autoclave, has been scaled up by an original approach to kg/month production rate [21].

In all these devices it is important to assess the mechanical properties of the final system (for example in a water filter weaved from titanate nanowires) which depend on the properties of the single fibers. Also, there is a significant interest to extend the applicability of titania thin films to flexible substrates in dye-sensitized solar cell (DSSC) [22–24], supercapacitors [25], perovskite solar cell [26,27], gas sensors [28]. In these applications, the preparation of porous, uniform and crack-free nanoparticle-based films is particularly challenging due to the intrinsic rigidity of sintered titania, ultimately deteriorating the performance values of lab-scale prototype devices. The effect of particle

shape, replacing isotropic particles with highly anisotropic, fiber-like particles may open new avenues for the long-sought satisfactory electronic and mechanical performance metrics of flexible devices.

Here, we report a detailed study of the mechanical response of titanate nanowires: their elastic and shear moduli, their flexibility, fatigue behavior and the rupture force. We also characterize the change of Young's modulus due to the thermal transformation of titanate into anatase NWs.

### 2. Experimental methods

#### 2.1. Titanate material and fabrication

Protonated titanate nanowire ( $\text{H}_2\text{Ti}_3\text{O}_7$ ) were prepared by a two-step hydrothermal process; the typical synthesis procedure, which results in single-crystalline nanowires, is described elsewhere [29]. A large assembly of them is shown on an Transmission Electron Microscope (TEM) image in Fig. 1(a). They have belt-like shape and their width ranges from 10 to 100 nm and their length can go up tens of  $\mu\text{m}$  [30]. On the High Resolution-Transmission Electron Microscope (HR-TEM) image of Fig. 1(b), one can clearly notice the layered structure of the NWs. This observation of the gallery spacing is feasible when the belt-like nanowire is laying in a tilted position, with its thinner sides on the substrate. It is more frequent that the nanowires are attached with their wider base on a given substrate. It is important to point out, that this latter scenario, when the nanobelts layer planes are in parallel with the surface is chosen for this study. The layered structure has been confirmed by TEM image and the corresponding electron diffraction

\* Corresponding author. EPFL SB IPHYS LPMC PH D2 355 (Bâtiment PH) Station 3 CH-1015, Lausanne, Switzerland.  
E-mail address: [lidia.rossi@epfl.ch](mailto:lidia.rossi@epfl.ch) (L. Rossi).

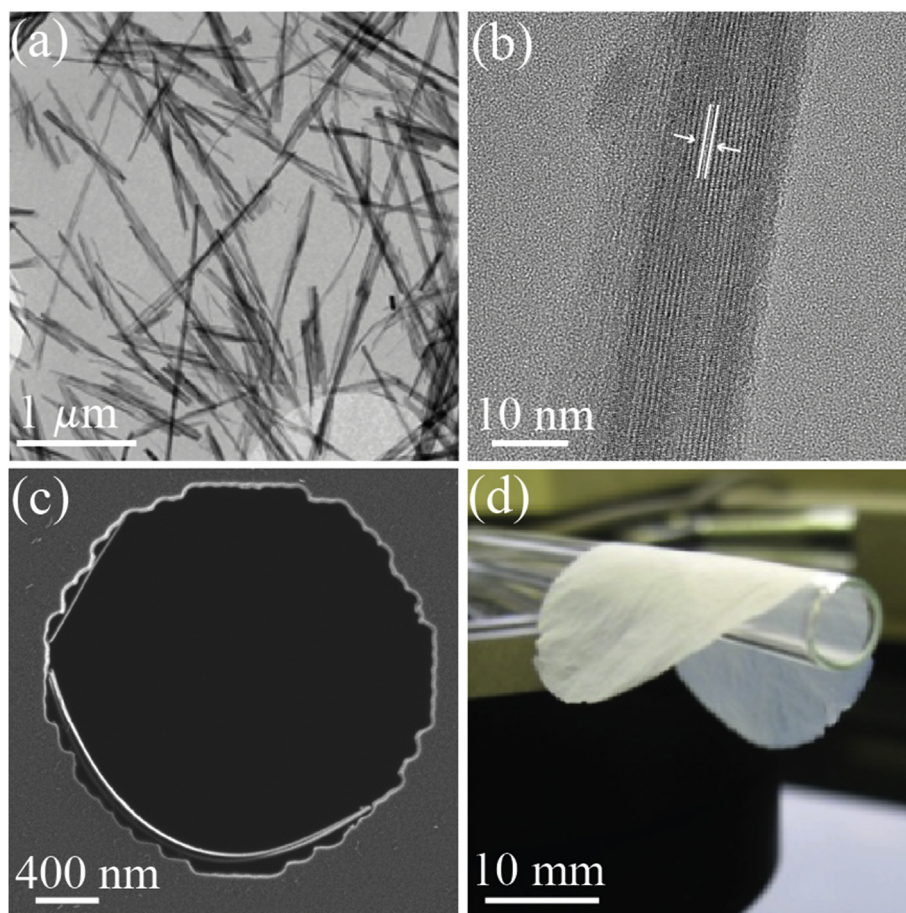


**Fig. 1.** (a) TEM image of a large assembly titanate NW ( $\text{H}_2\text{Ti}_3\text{O}_7$ ). (b) HR-TEM image showing the layered and single crystalline nature of the NW. (c) The highly elastic character of the NW is shown by adopting the shape of a hole made in silicon. (d) A membrane made of titanate NW.

pattern showing a crystalline structure with a gallery spacing of 0.7 nm (see Fig. 1(b) and Fig. S1). The high crystallinity and concomitant high flexibility could be seen in Fig. 1(c), where an individual NW, deposited from suspension on a membrane, adopts to the curvature of the hole. This high flexibility of the titanate NW allows making highly functional membranes from them (see Fig. 1(d) and Horváth et al. [17]).

## 2.2. Titanate characterization

Titanate NW were characterized by an Scanning Electron Microscope (SEM, Zeiss Merlin, Gemini II column) to localize and observe the morphology of nanowires. SEM images were acquired at an accelerating voltage of 2 kV and 150 pA electron beam current. TEM image was performed at 200 kV high voltage on a FEI Talos microscope in bright field.

An Atomic Force Microscope (AFM, XE-100 PSIA) operating in air was used to investigate the surface topography and to apply a load to the NWs in order to determine directly the resulting.

## 2.3. AFM and cantilever calibration

To provide accurate nanomechanical property measurements, both, the cantilever spring constant and the deflection sensitivity are required. Conventional spring constant calibration techniques rely on multiple cantilever probe tip contacts to the surface with the consequences of damaging the tip. Therefore, we preferred to use commercially available cantilevers, laser Doppler vibrometry (LDV) calibrated, RTESPA-300-30 from Bruker. We have chosen a cantilever type with high nominal 40 N/m spring constant and 30 nm tip end radius,

specifically calibrated for our experiments. The results shown in this article were obtained with a 47.038 N/m spring constant and 30.1 nm tip end radius cantilever. An SEM image of the tip used for the measurements is shown in Fig. S2. The AFM (XE-100 PSIA) used a 2-dimensional flexure stage to scan the sample in the XY direction, and a stacked piezoelectric actuator to scan the probe in the Z direction. In this way, the accurate position of the probe was ensured while eliminating the crosstalk issues commonly faced in such measurements. The deflection sensitivity is determined from a force versus piezo extension curve on a stiff substrate in the linear region of both stacked piezoelectric actuator and deflection detector.

## 2.4. Mechanical characterization method

In order to carry out mechanical characterization of NWs, we applied the three points bending measurement method using an AFM in conjunction with the so-called “Swiss cheese method” as first proposed by J. P. Salvetat and colleagues [31,32] for carbon nanotubes. The configuration is the following: on e-beam lithography defined holes in a silicon substrate (800 nm diameter and 400 nm depth), individual titanate NWs are deposited from an ultrasonicated suspension via a stamping method. First, the nanowire suspension was filtered on a Teflon membrane and subsequently stamped against the micro-fabricated hole-containing silicon substrate. Due to the wettability differences of the substrates, the nanowires were preferentially transferred to the silicon substrate with high yield. After the evaporation of the remaining isopropanol, the NWs’ adhesion to the silicon substrate is strong, so they can be treated as a double clamped beams of suspended length  $L$  (see Fig. 2(a)) [32]. This strong attachment is caused by

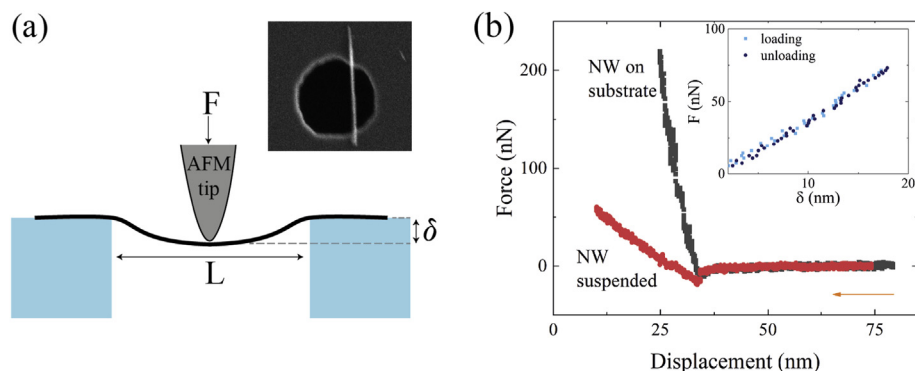


**Fig. 2.** Experimental configuration for measuring the elastic response of titanate NWs. (a) Sketch of the three-point bending test by AFM, indicating the major parameters for the evaluation: the inset shows an SEM image of the suspended NW over the lithographically defined hole in silicon. (b) Applied force versus displacement for the three-point bending test. The black line, the reference curve, measured on the NW supported by the solid substrate; while red line is recorded in the middle of the hole. The deflection  $\delta$ , used for the calculation of the bending modulus in equation (1), is extracted as the difference between the red and black curves at a given force, as shown in the inset. (For interpretation of the references to colour in this figure legend, the reader is referred to the Web version of this article.)

adhesion, as well as hydroxyl bond formation between the titanate and native silicon oxide layer, and is clearly demonstrated during extended AFM imaging, where no displacement of the portion lying on the substrate is observed. This is also illustrated in Fig. S3 from the repeatability test by applying a force-release cycle 300-times, where no movement of the suspended NW was observed.

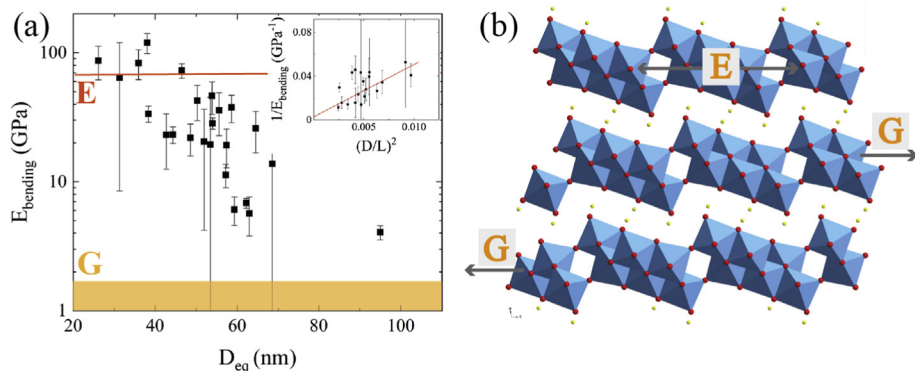
SEM images show that the NWs possess a typical rectangular cross-section (of width  $b$ , and height  $h$ ), and lay over the substrate with their wider surface. More details are explained in the Supplementary Material and Fig. S4. In this model, of a double clamped beam [33] the bending modulus ( $E_b$ ) is related to the deflection  $\delta$  via the moment of inertia  $I$  of the NW, to the suspended length and to the loading force  $F$  according to the following relationship:

$$E_b = \frac{FL^3}{192\delta I}, \quad (1)$$

where  $I = bh^3/12$  for rectangular cross-section beams.

One has to notice that the bending modulus has a strong dependence on the NW dimensions ( $L$ ,  $b$ ,  $h$  – the suspended length, width and height, respectively). Although AFM is a high precision tool, small uncertainty could add up a high error bar, in the range of 20–30 [31,32].

The bending data were collected in the following way. After the deposition of the suspension of titanate NW on the silicon substrate with the array of holes and the evaporation of the liquid, the surface was imaged in a non-contact AFM mode. In cases, where NWs were bridging a hole, force-displacement measurements were taken in contact AFM mode. For each NW, before measuring the deflection on the hole, we carried out spectroscopy on the part laying on the substrate; this measurement served as a reference (black curve in Fig. 2(b)). Then the same measurement was taken in the middle of the NW suspended on the hole. Both force-displacement measurements were taken with a speed of 0.3  $\mu\text{m/s}$ . The difference in position, i.e. of the displacement signal, for the same applied force between the two measurements define the actual deflection  $\delta$ , as plotted in the inset of Fig. 2(b). The  $E_b$  is



calculated from the slope of the linear regression of the  $F$ - $\delta$  graph according to equation (1). The suspended length and the cross-section of the NWs varied considerably for each sample.

In the case of a uniform beam, with negligible shear,  $E_b$  coincides with the Young's modulus  $E$ . If there are subunits in the beam, which can slide on each other under the loading force, then both  $E$  and  $G$ , the shear modulus, influence  $E_b$ . In this case the extraction of the moduli requires a more careful data analysis, where the bending is measured for various diameters ( $D$ ) and suspended lengths ( $L$ ). In this case, one can extract the two moduli ( $E$  and  $G$ ) using the following relation [33]:

$$\frac{1}{E_b} = \frac{1}{E} + \frac{10}{3} \frac{1}{G} \frac{D^2}{L^2} \quad (2)$$

This analysis was successfully applied for single-walled carbon nanotube bundles in which the individual nanotubes are held together with weak Van der Waals forces. The obtained values were  $E = 1$  TPa and  $G = 5$  GPa [32]. Upon electron irradiation, the nanotubes got cross-linked and  $G$  tremendously increased [34].

### 3. Results and discussion

#### 3.1. Mechanical properties

Fig. 3(a) displays the measured  $E_b$  for a large assembly of NWs. Surprisingly, it has a strong cross-section (translated into equivalent diameter) dependence. Actually, we have considerable bending due to the weak interaction between the layers in the structure. In consequence, shear contribution plays an important role in the mechanical response of NWs. In the spirit of equation (2), shear is important when:  $L/R \leq 4\sqrt{E/G}$  [33]. In our case,  $L/R$  ranges from 7.5 to 20 (evaluated by SEM and AFM measurements), so the ratio of  $E/G$  should be above 25. Using equation (2), the two moduli are deconvoluted in the following way.

The titanate NWs have rectangular cross-section, of aspect ratio width/height between 0.7 and 2, that can be conveniently

**Fig. 3.** (a) Measured bending modulus  $E_b$  for 25 different titanate NWs with different equivalent diameters between 26 and 95 nm; in the inset the  $1/E_b$  as a function of  $(D/L)^2$  for determination of  $E$  and  $G$ , according to equation (2). (b) Sketch of the crystal structure of titania NW, in order to illustrate the  $E$  and  $G$  moduli extracted from the left panel.

characterized by an equivalent diameter,  $D_{eq}$ . The use of  $D_{eq}$  permits a more direct comparison with the results of other authors obtained on nanowires with circular cross-section. The  $E_b$  values shown in Fig. 3(a) for 25 titanate NWs as a function of the  $D_{eq}$  were calculated from the linear part of the ( $F$ - $\delta$ ) curves, typically restricted to the 50–150 nN force range (or 25–35 nm displacement range), well below the rupture point. The reason for not going too high in loading, was to avoid damaging the NWs, which were later submitted to thermal treatment, to transform them into anatase, of single-crystalline structure. Making use of equation (2), the plot of  $1/E_b$  versus  $D^2/L^2$  in the inset to Fig. 3(a) allows to extract  $E$  and  $G$ . The slope gives  $G$  while the intercept gives directly  $1/E$ . We obtained:  $G = 1.5 \pm 0.8$  GPa and  $E = 66.7 \pm 25$  GPa. Despite the considerable error bar the presence of  $G$  (of a non-zero slope) is evident in these measurements.

Other publications on  $\text{Na}_2\text{Ti}_3\text{O}_7$  NWs, report an elastic modulus  $E$  for the NWs of  $33 \pm 7$  GPa [35] and between 37 and 250 GPa [36]. We believe that their low value and the large dispersion is due the presence of shear modulus in their measurements. To our knowledge, our result is amongst the first ones to report  $G$  for layered titanate NWs. We illustrate this new notion found for our system in Fig. 3(b), which could be important for other layered or composite nanostructures too. The only other report on the mechanical response of layered titanate nanoribbons is that of Humar et al. [37] which values are however surprising:  $E$  reaches 400 GPa, but  $G$  is in the 0.01 GPa range (hundred times smaller than ours). Actually, the very low value for  $G$  is coming from the shear modulus between nanoribbons in a bundle, and not that within a ribbon, measured in this work.

It has to be mentioned that the  $E$  vs diameter trend shown in Fig. 3(a) is similar to the one reported by Chen et al. [38], for ZnO NWs. Beyond the fact that they have covered a broader diameter range, the ZnO has no layered structure, so they attribute the decrease of the modulus to binding energy balance in a core-shell model. However, we underline that in our case the mechanism causing the decrease of flexural modulus is different from that of Chen et al. It is due to the intrinsic layered structure of our nanowires and the size-dependent convolution of the shear between layers to the overall response.

### 3.2. Fatigue

If one is dealing with functional NWs, exposed to repeated mechanical loadings, it is important to check the fatigue of the material. A NW was submitted to a fatigue cycle with the result shown in Fig. 4(a). The red curve represents the first 600 force-release cycle up to  $F = 300$  nN. The overlap of different cycles is remarkable: the NW did 600 cycles and still remained perfectly elastic, with the absence of noticeable hysteresis. The following cycles, in turquoise for the load and blue for the unload, show a lower force than previous one (red) for the same displacement and a marked hysteresis. In the subsequent #602 loading/

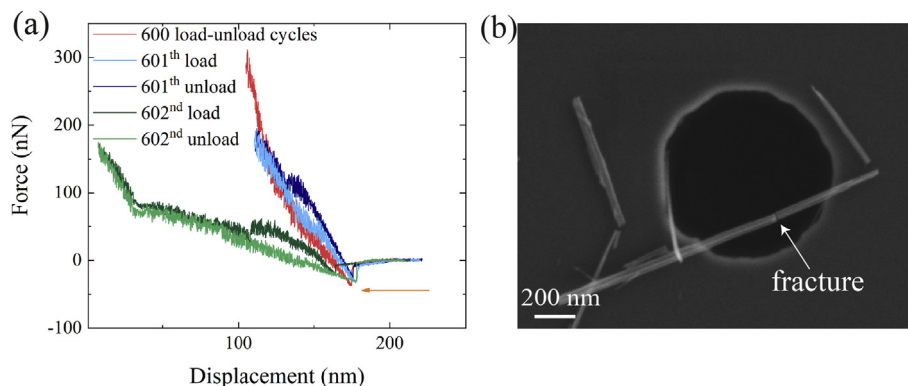


Fig. 4. Fatigue-test of the titanate NW. (a) The force – release cycle has been applied multiple times, showing the gradual decrease of the slope (stronger and stronger deflection) due to the consecutive ruptures of the titanate layers, until the final rupture of the NW. (b) SEM image showing the rupture in the middle of the NW.

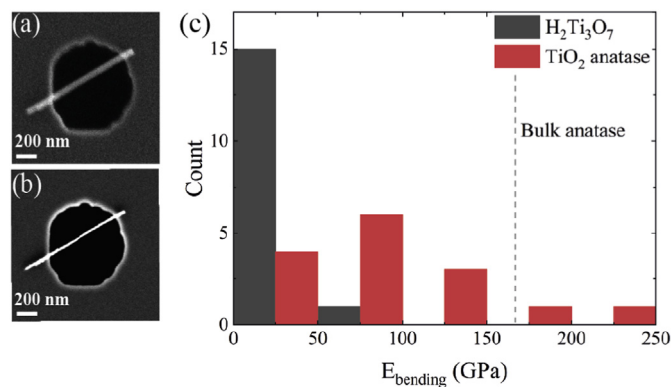


Fig. 5. SEM image of a typical titanate NW (a) Before and (b) after the thermal treatment at 800 °C which transforms it into the anatase phase. (c) Histogram of the bending modulus ( $E_b$ ) measured on 15 NWs in the titanate and anatase forms.

unloading cycle (dark green for the loading and light green for unloading) one can observe a dramatic change in the bending modulus with a drop of factor 3. We interpret these changes as a gradual rupture of the layers upon mechanical loadings composing the NWs. Presumably, the shear, translated into friction between the layers has a role in the breaking of the individual layers. In the end, the sample did not oppose any resistance to the AFM tip, the NW was ruptured. The SEM image in Fig. 4(b) illustrates the end result.

### 3.3. Transformation of titanate into anatase

After full characterization of the titanate NWs at room temperature, they were submitted to a thermal treatment up to 800 °C in air in order to transform them into anatase polymorph of  $\text{TiO}_2$ . The temperature ramp rate was 20 °C/min and the samples were kept at 800 °C for 1 h. One has to observe, that at such a high-temperature, usually the bulk anatase transforms into rutile polymorph. But our structural investigations show that the anatase nanowires preserve their structure even at this high-temperature [42]. A representative SEM imaging of this transformation is shown in (a) (titanate) and Fig. 5(b) (anatase). The shrinkage of the NW upon this transformation is clearly visible, since the layered texture is lost and the anatase has a uniform structure. Shrinkage due to recrystallization into the anatase phase introduces mechanical stresses in the structure, enhanced by the mismatch of NW-substrate thermal expansion coefficient and despite great care in handling, only 15 out of 25 samples survived the heat treatment.

These were exposed again to bending measurements, and the values of  $E_b$  are reported in Fig. 5(c), where for the sake of comparison, the titanate NWs are plotted, as well. One can notice that  $E_b$  is much higher

for the anatase NWs, due to the absence of the shear modulus in the mechanical response, so  $E_b$  corresponds to  $E$ . It is known from indentation measurement, that for the bulk, anatase single crystal  $E = 167 \pm 15$  GPa [39]. Recent atomistic simulations of mechanical deformation of anatase sample performed on an assembly of nanocrystalline grains of 2–6 nm in size, resulted in Young's modulus in the 170–200 GPa range [40]. Our anatase NWs cover this range, although the high abundance of lower values testify that during the recrystallization a considerable amount of defects were created, which reduce its mechanical response.

### 3.4. Superelasticity of titanate NWs

The surprising observation of the super elastic behavior of the titanate nanowire shown in Fig. 1(c), inferring a radius of curvature of 1.5–2.5  $\mu\text{m}$  merits few words. It has to be mentioned that this behavior is not restricted to titanate NWs, but has been observed for other NWs as well (gold NWs [41],  $\text{CH}_3\text{NH}_3\text{PbI}_3$  NWs [39]). In our view, this necessitates the absence of grain boundaries, of dislocation which would cause a departure from the elastic behavior and would result in a higher fragility. It means that a good number of our titanate NWs (without improved statistics) have a high structural quality.

## 4. Conclusion

In conclusion, we performed mechanical measurements on titanate NWs using an AFM-based bending test. In this layered structured material, we have given evidence of the presence of a low shear modulus of  $G = 1.5 \pm 0.8$  GPa, which strongly influences the mechanical response of these NWs, despite the high  $E$  of  $67 \pm 25$  GPa. The low  $G$  may play a role in the fatigue of the NWs. The thermal transformation and recrystallization of the titanate into anatase NWs, without shear behavior, increases  $E$  towards the bulk value.

Owing to the low radius of curvature coupled with superior mechanical strength of titanate and anatase nanowires against repetitive bending stress conditions, these materials may serve as building blocks of future flexible energy devices, environmental decontamination systems, super thermal-insulators, sensors, catalyst supports and fiber-reinforced plastics, metals and ceramics.

### Declaration of competing interest

The authors declare that they have no known competing financial interests or personal relationships that could have appeared to influence the work reported in this paper.

### Acknowledgments

The discussion of the superelastic behavior of NWs with Dr. D. Mari and the support of pre-launched Swoxid SA are greatly acknowledged. We thank the technical help of Dr. N. Jomaa, Dr. L. Ćirić, V. Nussbaumer, and Dr. M. Spina as well as the CIME-EPFL for access to the electron microscopes.

### Appendix A. Supplementary data

Supplementary data to this article can be found online at <https://doi.org/10.1016/j.ceramint.2020.04.077>.

## References

- [1] U. Diebold, The surface science of titanium dioxide, *Surf. Sci. Rep.* 48 (2003) 53–229, [https://doi.org/10.1016/S0167-5729\(02\)00100-0](https://doi.org/10.1016/S0167-5729(02)00100-0).
- [2] L.G. Phillips, D.M. Barbano, The influence of fat substitutes based on protein and titanium dioxide on the sensory properties of lowfat milks, *J. Dairy Sci.* 80 (1997) 2726–2731, [https://doi.org/10.3168/jds.S0022-0302\(97\)76234-9](https://doi.org/10.3168/jds.S0022-0302(97)76234-9).
- [3] B. O'Regan, M. Grätzel, A low-cost, high-efficiency solar cell based on dye-sensitized colloidal  $\text{TiO}_2$  films, *Nature* 353 (1991) 737–740, <https://doi.org/10.1038/353737a0>.
- [4] D. Gust, T.A. Moore, A.L. Moore, Mimicking photosynthetic solar energy transduction, *Acc. Chem. Res.* 34 (2001) 40–48, <https://doi.org/10.1021/ar9801301>.
- [5] R.L. Pozzo, M.A. Baltanás, A.E. Cassano, Supported titanium oxide as photocatalyst in water decontamination: state of the art, *Catal. Today* 39 (1997) 219–231, [https://doi.org/10.1016/S0920-5861\(97\)00103-X](https://doi.org/10.1016/S0920-5861(97)00103-X).
- [6] R.W. Matthews, Photooxidation of organic impurities in water using thin films of titanium dioxide, *J. Phys. Chem.* 91 (1987) 3328–3333, <https://doi.org/10.1021/j100296a044>.
- [7] S. Malato, P. Fernández-Ibáñez, M.I. Maldonado, J. Blanco, W. Gernjak, Decontamination and disinfection of water by solar photocatalysis: recent overview and trends, *Catal. Today* 147 (2009) 1–59, <https://doi.org/10.1016/j.cattod.2009.06.018>.
- [8] A. Fujishima, T.N. Rao, D.A. Tryk,  $\text{TiO}_2$  photocatalysts and diamond electrodes, *Electrochim. Acta* 45 (2000) 4683–4690, [https://doi.org/10.1016/S0013-4686\(00\)00620-4](https://doi.org/10.1016/S0013-4686(00)00620-4).
- [9] A. Fujishima, K. Hashimoto, T. Watanabe,  *$\text{TiO}_2$  Photocatalysis: Fundamentals and Applications*, Bkc, Tokyo, 1999.
- [10] K. Nakata, A. Fujishima,  $\text{TiO}_2$  photocatalysis: design and applications, *J. Photochem. Photobiol. C Photochem. Rev.* 13 (2012) 169–189, <https://doi.org/10.1016/j.jphotochemrev.2012.06.001>.
- [11] D.B. Strukov, G.S. Snider, D.R. Stewart, R.S. Williams, The missing memristor found, *Nature* 453 (2008) 80–83, <https://doi.org/10.1038/nature06932>.
- [12] P.K. Dutta, A. Ginwalla, B. Hogg, B.R. Patton, B. Chwieroth, Z. Liang, P. Gouma, M. Mills, S. Akbar, Interaction of carbon monoxide with anatase surfaces at high Temperatures: optimization of a carbon monoxide sensor, *J. Phys. Chem. B* 103 (1999) 4412–4422, <https://doi.org/10.1021/jp9844718>.
- [13] M.M. Arafat, B. Dinan, S.A. Akbar, A.S.M.A. Haseeb, Gas sensors based on one dimensional nanostructured metal-oxides: a review, *Sensors* 12 (2012) 7207–7258, <https://doi.org/10.3390/s120607207>.
- [14] H. Wu, C. Xu, J. Xu, L. Lu, Z. Fan, X. Chen, Y. Song, D. Li, Enhanced supercapacitance in anodic  $\text{TiO}_2$  nanotube films by hydrogen plasma treatment, *Nanotechnology* 24 (2013) 455401, <https://doi.org/10.1088/0957-4484/24/45/455401>.
- [15] M. Salari, K. Konstantinov, H. Kun Liu, Enhancement of the capacitance in  $\text{TiO}_2$  nanotubes through controlled introduction of oxygen vacancies, *J. Mater. Chem.* 21 (2011) 5128–5133, <https://doi.org/10.1039/C0JM04085A>.
- [16] J. Xu, C. Jia, B. Cao, W.F. Zhang, Electrochemical properties of anatase  $\text{TiO}_2$  nanotubes as an anode material for lithium-ion batteries, *Electrochim. Acta* 52 (2007) 8044–8047, <https://doi.org/10.1016/j.electacta.2007.06.077>.
- [17] E. Horváth, P.R. Ribić, F. Hashemi, L. Forró, A. Magrez, Dye metachromasy on titanate nanowires: sensing humidity with reversible molecular dimerization, *J. Mater. Chem.* 22 (2012) 8778–8784, <https://doi.org/10.1039/C2JM16443D>.
- [18] M.T. Byrne, J.E. McCarthy, M. Bent, R. Blake, Y.K. Gun'ko, E. Horváth, Z. Konya, A. Kukovecz, I. Kiricsi, J.N. Coleman, Chemical functionalisation of titania nanotubes and their utilisation for the fabrication of reinforced polystyrene composites, *J. Mater. Chem.* 17 (2007) 2351–2358, <https://doi.org/10.1039/B612886F>.
- [19] X. Mettan, J. Jaćimović, O.S. Barisić, A. Pisoni, I. Batistić, E. Horváth, S. Brown, L. Rossi, P. Szirmai, B. Farkas, H. Berger, L. Forró, Tailoring thermal conduction in anatase  $\text{TiO}_2$ , *Commun. Phys.* 2 (2019), <https://doi.org/10.1038/s42005-019-0224-7>.
- [20] P. Hernández-Hipólito, M. García-Castillejos, E. Martínez-Klimova, N. Juárez-Flores, A. Gómez-Cortés, T.E. Klimova, Biodiesel production with nanotubular sodium titanate as a catalyst, *Catal. Today* 220–222 (2014) 4–11, <https://doi.org/10.1016/j.cattod.2013.09.003>.
- [21] E. Horváth, L. Forró, A. Magrez, Titanium Oxide Aerogel Composites, EP2964577A1, 2016, <https://patents.google.com/patent/EP2964577A1/en> accessed December 17, 2019.
- [22] Y. Xiao, J. Wu, G. Yue, G. Xie, J. Lin, M. Huang, The preparation of titania nanotubes and its application in flexible dye-sensitized solar cells, *Electrochim. Acta* 55 (2010) 4573–4578, <https://doi.org/10.1016/j.electacta.2010.03.011>.
- [23] D. Zhang, J.A. Downing, F.J. Knorr, J.L. McHale, Room-temperature preparation of nanocrystalline  $\text{TiO}_2$  films and the influence of surface properties on dye-sensitized solar energy conversion, *J. Phys. Chem. B* 110 (2006) 21890–21898, <https://doi.org/10.1021/jp0640880>.
- [24] X. Li, H. Lin, J. Li, N. Wang, C. Lin, L. Zhang, Chemical sintering of graded  $\text{TiO}_2$  film at low-temperature for flexible dye-sensitized solar cells, *J. Photochem. Photobiol. Chem.* 195 (2008) 247–253, <https://doi.org/10.1016/j.jphotochem.2007.10.010>.
- [25] J. Zhi, C. Yang, T. Lin, H. Cui, Z. Wang, H. Zhang, F. Huang, Flexible all solid state supercapacitor with high energy density employing black titania nanoparticles as a conductive agent, *Nanoscale* 8 (2016) 4054–4062, <https://doi.org/10.1039/C5NR08136J>.
- [26] Y. Dkhissi, F. Huang, S. Rubanov, M. Xiao, U. Bach, L. Spiccia, R.A. Caruso, Y.-B. Cheng, Low temperature processing of flexible planar perovskite solar cells with efficiency over 10%, *J. Power Sources* 278 (2015) 325–331, <https://doi.org/10.1016/j.jpowsour.2014.12.104>.
- [27] D. Liu, T.L. Kelly, Perovskite solar cells with a planar heterojunction structure prepared using room-temperature solution processing techniques, *Nat. Photon.* 8 (2014) 133–138, <https://doi.org/10.1038/nphoton.2013.342>.
- [28] N.-S. Jang, M.S. Kim, S.-H. Kim, S.-K. Lee, J.-M. Kim, Direct growth of titania nanotubes on plastic substrates and their application to flexible gas sensors, *Sensor. Actuator. B Chem.* 199 (2014) 361–368, <https://doi.org/10.1016/j.snb.2014.03.113>.
- [29] N. Tétreault, E. Horváth, T. Moehl, J. Brillet, R. Smajda, S. Bungener, N. Cai,

- P. Wang, S.M. Zakeeruddin, L. Forró, A. Magrez, M. Grätzel, High-efficiency solid-state dye-sensitized solar cells: fast charge extraction through self-assembled 3D fibrous network of crystalline TiO<sub>2</sub> nanowires, *ACS Nano* 4 (2010) 7644–7650, <https://doi.org/10.1021/nn1024434>.
- [30] E. Horváth, I. Szilágyi, L. Forró, A. Magrez, Probing titanate nanowire surface acidity through methylene blue adsorption in colloidal suspension and on thin films, *J. Colloid Interface Sci.* 416 (2014) 190–197, <https://doi.org/10.1016/j.jcis.2013.10.049>.
- [31] J.-P. Salvetat, A.J. Kulik, J.-M. Bonard, G.A.D. Briggs, T. Stöckli, K. Méténier, S. Bonnamy, F. Béguin, N.A. Burnham, L. Forró, Elastic modulus of ordered and disordered multiwalled carbon nanotubes, *Adv. Mater.* 11 (1999) 161–165, [https://doi.org/10.1002/\(SICI\)1521-4095\(199902\)11:2<161::AID-ADMA161>3.0.CO;2-J](https://doi.org/10.1002/(SICI)1521-4095(199902)11:2<161::AID-ADMA161>3.0.CO;2-J).
- [32] J.-P. Salvetat, G.A.D. Briggs, J.-M. Bonard, R.R. Bacsá, A.J. Kulik, T. Stöckli, N.A. Burnham, L. Forró, Elastic and shear moduli of single-walled carbon nanotube ropes, *Phys. Rev. Lett.* 82 (1999) 944–947, <https://doi.org/10.1103/PhysRevLett.82.944>.
- [33] J.M. Gere, S.P. Timoshenko, *Mechanics of Materials*, PWS Publishing Company, Boston, MA, 1990.
- [34] A. Kis, G. Csányi, J.-P. Salvetat, T.-N. Lee, E. Couteau, A.J. Kulik, W. Benoit, J. Brugger, L. Forró, Reinforcement of single-walled carbon nanotube bundles by intertube bridging, *Nat. Mater.* 3 (2004) 153–157, <https://doi.org/10.1038/nmat1076>.
- [35] A. Bo, H. Zhan, J. Bell, H. Zhu, Y. Gu, Mechanical bending properties of sodium titanate (Na<sub>2</sub>Ti<sub>3</sub>O<sub>7</sub>) nanowires, *R. Soc. Chem.* 4 (2014) 56970–56976, <https://doi.org/10.1039/c4ra11753k>.
- [36] A. Bo, K. Chen, E. Pickering, H. Zhan, J. Bell, A. Du, Y. Zhang, X. Wang, H. Zhu, Z. Shan, Y. Gu, Atypical defect motions in brittle layered sodium titanate nanowires, *J. Phys. Chem. Lett.* 9 (2018) 6052–6059, <https://doi.org/10.1021/acs.jpcclett.8b02349>.
- [37] M. Humar, D. Arčon, P. Umek, M. Škarabot, I. Mušević, G. Bregar, Mechanical properties of titania-derived nanoribbons, *Nanotechnology* 17 (2006) 3869–3872, <https://doi.org/10.1088/0957-4484/17/15/043>.
- [38] C.Q. Chen, Y. Shi, Y.S. Zhang, J. Zhu, Y.J. Yan, Size dependence of Young's modulus in ZnO nanowires, *Phys. Rev. Lett.* 96 (2006) 075505, <https://doi.org/10.1103/PhysRevLett.96.075505>.
- [39] L. Ciric, Unpublished, n.d., personal communication.
- [40] X. Zhang, H. Gao, X. Li, Atomistic simulations of superplasticity and amorphization of nanocrystalline anatase TiO<sub>2</sub>, *Extreme Mech. Lett.* 22 (2018) 131–137, <https://doi.org/10.1016/j.eml.2018.05.009>.
- [41] B. Wu, A. Heidelberg, J.J. Boland, Mechanical properties of ultrahigh-strength gold nanowires, *Nat. Mater.* 4 (2005) 525–529, <https://doi.org/10.1038/nmat1403>.
- [42] L. Rossi, X. Berdat, M. Spina, S. Brown, S. Katrych, L. Forró, E. Horváth, Thermal coarsening of individual titanate nanowires and their assemblies: surface vs. bulk diffusion, *Ceram. Int.* (2020), <https://doi.org/10.1016/j.ceramint.2020.03.189>.